Transient CFD Validation for Air–Water Two-Phase Flow in a Helical Coil Using Void Fraction Measurements

Janghun Han, Minseop Song*
Department of Nuclear Engineering, Hanyang University, 222, Wangsimni-ro, Seongdong-gu, Seoul, 04761, Republic of Korea
** Corresponding author: hysms@hanyang.ac.kr*

***Keywords : Helical coil, Two-phase flow, CFD validation, VOF**

1. Introduction

Helical coils have been widely adopted in heat exchangers and steam generator designs for small modular reactor (SMR) systems because of their compact geometry and superior heat transfer performance. This adoption is supported by prior single-phase heat-exchanger studies showing a clear thermal–hydraulic trade-off in helical geometries. Prabhanjan et al. [1] reported that the heat transfer coefficient of a helical coil was approximately 1.16 and 1.43 times that of a straight tube at 40°C and 50°C, respectively, while a more recent comparative study(Flayyih et al. [2]) reported an 8–12% increase in Nusselt number for a helical coil with a corresponding pressure-drop increase of up to 20% under matched conditions. In such systems, the predictive reliability of internal flow behavior, particularly two-phase flow behavior, is directly related to thermal performance, operational stability, and safety. Therefore, a quantitative understanding of flow characteristics in helical coils is essential.

However, two-phase flow in a helical coil behavior from that in a straight tube. The curvature and torsion of the coil generate centrifugal effects and secondary flow, which can produce asymmetric phase distributions over the cross-section and complex time dependent flow structures. As a result, intuitive interpretations or thermal-hydraulic correlations developed for straight tubes may not be directly applicable to helical coils, especially under high curvature or high torsion conditions, and their practical applicability may be limited. Moreover, the resulting flow behavior is highly sensitive to coil geometry, including curvature, pitch, tube diameter, and cross-sectional shape. Thus, experimental findings obtained for a specific coil geometry are not readily generalized to other geometries. Thus, experimental findings obtained for specific coil geometry are not readily generalized to other geometries.

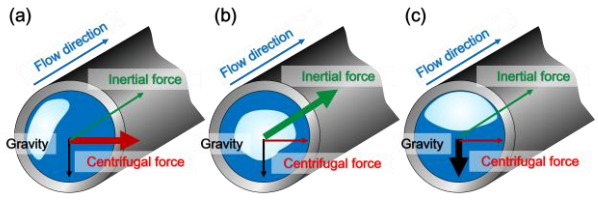

Figure 1. Schematic of dominant forces affecting bubble behavior in a helical coil

Against this background, experimental studies on two-phase flow in helical coils have been continuously reported. Zhu et al. [3] combined a double-sensor conductivity probe and a high-speed camera to identify six flow regimes in a helical coil and proposed quantitative criteria for flow regime transitions. Zhu et al. [4] further investigated intermittent flow and showed that the cross-sectional void fraction distribution exhibits a rotating biased structure, while the Dean vortex affects slug length and frequency, thereby linking observed flow behavior to mechanism-based indicators. More recently, Breitenmoser et al. [5] employed high speed X-ray radiography to provide quantitative void fraction images, temporal evolution, cross-sectional profiles, and Probability Density Function (PDF) based features, emphasizing the importance of high-quality void fraction data for the analysis and validation of helical coil two-phase flow. Depending on the relative dominance of centrifugal, inertial, and gravitational forces, bubble behavior in a helical coil may vary significantly, leading to different cross-sectional phase distributions and flow structures, as schematically illustrated in Figure 1.

Despite these efforts, practical and methodological limitations remain in the quantitative validation of two-phase flow in helical coils. High-resolution void fraction measurements are difficult to obtain because of limitations in instrumentation and post processing procedures, and CFD also faces challenges because appropriate mesh resolution and timestep settings may vary depending on the flow regime, making it difficult to apply a single numerical setup uniformly over a wide operating range. In addition, many previous experimental–CFD comparisons have focused on macroscopic or section-averaged metrics, such as pressure drop and average heat transfer coefficients, which are not sufficient to fully validate the asymmetric cross-sectional phase distribution and time-dependent flow structures that are central to helical coil two-phase flow. Meanwhile, such asymmetric phase distributions and flow regime transitions can be directly related to system performance and reliability, and it is not realistic to conduct experiments for all possible geometries and operating conditions. Therefore, to utilize CFD as a practical design and validation tool, it is necessary to define the applicable range of quantitative validation using not only averaged metrics but also phenomenon-based indicators such as time-resolved void fraction data.

The objective of this study is to perform a stepwise quantitative comparison and validation of transient CFD predictions against experimentally obtained void fraction data for air–water two-phase flow in a helical coil over multiple flow regimes from Breitenmoser et al. [5]. In particular, this study goes beyond conventional average value-based comparisons by using time–void fraction data to evaluate the capability of CFD to reproduce unsteady flow structures and asymmetric phase behavior in a helical coil, and to present a practical validation range for CFD-based analysis.

2. Methodology

2.1. Reference experiment

For the experimental basis of CFD validation, the present study used the X-ray void fraction data reported by Breitenmoser et al. (2021) for adiabatic upward air–water two-phase flow in a vertically oriented helical coil (MAHICan facility, ambient conditions). In reference experiment, the helical test section geometry was fixed, and the main operating variables were the superficial water and air velocities. The key geometric parameters of the helical coil used as the CFD reference are summarized in Table 1. These include the inner tube diameter, coil diameter, and helix angle, which define the curvature and torsion induced flow characteristics in the test section.

Table 1. Geometric parameters of the reference helical coil test section [5]

Helix diameter[m]	Pipe inner diameter[mm]	Helix angle[°]	Total length
1	12.57	14.3	7.92

Quantitative void fraction measurements in the reference study were obtained using high-speed X-ray radiography. The X-ray measurements were conducted 5.42 m downstream of the helical coil inlet (L/d=431) to minimize entrance effects, with a sampling frequency of 68.72 Hz and an exposure time of 0.1 ms. In the present study, four representative operating conditions (Cases 3, 6, 7, and 9 in Breitenmoser et al. [5]) were selected to assess CFD reproducibility over multiple flow regimes (plug, slug, and annular). The corresponding operating conditions and flow-regime labels used for the CFD simulations are summarized in Table 2.

Table 2. Reference experimental measurement result [5]

Case num	T [℃]	j_w [m/s]	j_a [m/s]	Flow regime
1	24.2	1.77	0.34	Plug
2	23.2	1.55	2.46	Slug
3	23.0	1.50	2.85	Slug
4	22.6	0.85	12.2	Annular

2.2. CFD model and boundary condition

Transient CFD simulations were conducted to reproduce the air–water two-phase flow in a helical coil under selected experimental conditions. All simulations were performed using ANSYS Fluent 2025 R2, employing an interface-capturing approach based on the coupled Level Set and Volume of Fluid (CLSVOF) model.

The two-phase flow was modeled using the Volume of Fluid (VOF) framework, in which a single conservation equation is solved for the mixture while the phase interface is tracked through the transport of volume fraction. The conservation of mass for the mixture is given by

$$\frac{\partial \rho}{\partial t} + \nabla \cdot (\rho u) = 0 \qquad (1)$$

where ρ and u denote the mixture density and velocity. The mixture density is evaluated from the phase volume fractions as

$$\rho = \alpha_g \rho_g + \alpha_l \rho_l, \qquad \alpha_g + \alpha_l = 1 \qquad (2)$$

with α_g and α_l representing the gas and liquid volume fractions, respectively. The momentum conservation equation for the mixture is expressed as

$$\frac{\partial (\rho u)}{\partial t} + \nabla \cdot (\rho u u) = -\nabla p + \nabla \cdot [\mu (\nabla u + \nabla u^T)] + \rho g + F_\sigma \quad (3)$$

where p is the pressure, μ is the mixture viscosity, g is the gravitational acceleration, and F_σ is the surface tension force modeled using the continuum surface force (CSF) formulation. Energy conservation was not considered, as the present study focuses on isothermal hydrodynamic behavior.

Turbulence effects were modeled using the k–ω SST model, which provides improved near-wall prediction capability. An Enhanced Wall Treatment (EWT) was employed to reduce reliance on empirical wall functions. The mesh was designed such that more than 90% of wall-adjacent cells satisfied $y^+<1$, ensuring sufficient resolution of the viscous sublayer.

The mesh topology and near-wall refinement strategy are illustrated in Figure 2(a), while the distribution of wall-adjacent cell y^+ values for a representative worst-case condition is shown in Figure 2(b). The computational domain consisted of a three-dimensional helical coil geometry identical to that of the reference experiment. The mesh was generated using SALOME 9.10.0, and the entire domain was discretized using a fully structured, all-hexahedral mesh. This approach ensured consistent grid alignment along the axial direction of the helical coil and improved numerical stability for transient two-phase simulations. The overall mesh structure, including axial mesh resolution, cross-sectional discretization, and near-wall inflation layers, is shown in Figure 2(a).

Boundary conditions and the gravitational direction are schematically illustrated in Figure 3. Gravity was applied in the -z direction of the Cartesian coordinate

system, corresponding to upward flow along the vertically oriented helical coil. At the inlet, experimental conditions were reported in terms of superficial velocities for each phase. Since the VOF model solves a single momentum equation for the mixture, the inlet velocity was prescribed as the mixture velocity, calculated from the superficial velocities as

$$U_m = j_g + j_l \tag{4}$$

where j_g and j_l denote the gas and liquid superficial velocities, respectively. The inlet gas volume fraction was then evaluated as

$$\alpha_{g,in} = \frac{j_g}{j_g + j_l} \tag{5}$$

and imposed at the inlet with respect to the gas phase. This approach assumes homogeneous phase transport at the inlet and provides a consistent means of specifying inlet conditions within the VOF framework. A pressure outlet boundary condition was applied at the outlet, and no-slip conditions were imposed on all solid walls.

All simulations were performed in a transient simulation. The time step was selected based on mesh and timestep sensitivity analyses, which are discussed separately. Constant thermophysical properties were assumed for both phases, and the surface tension coefficient was explicitly specified. The physical properties and key numerical parameters used in the simulations are summarized in Table 3.

Table 3. Fluid properties used in the CFD simulations

Property	Water	Air
Density [kg/m^3]	998.2	1.225
Dynamic viscosity [$Pa \cdot s$]	0.001003	1.78e-05
Surface tension [N/m]	0.072	

2.3. Mesh and timestep sensitivity analysis

To ensure numerical reliability in transient two-phase flow simulations, sensitivity analyses with respect to axial mesh resolution and timestep size were performed. The cross-sectional mesh resolution was fixed based on the near-wall requirement ($y^+ < 1$ for more than 90%

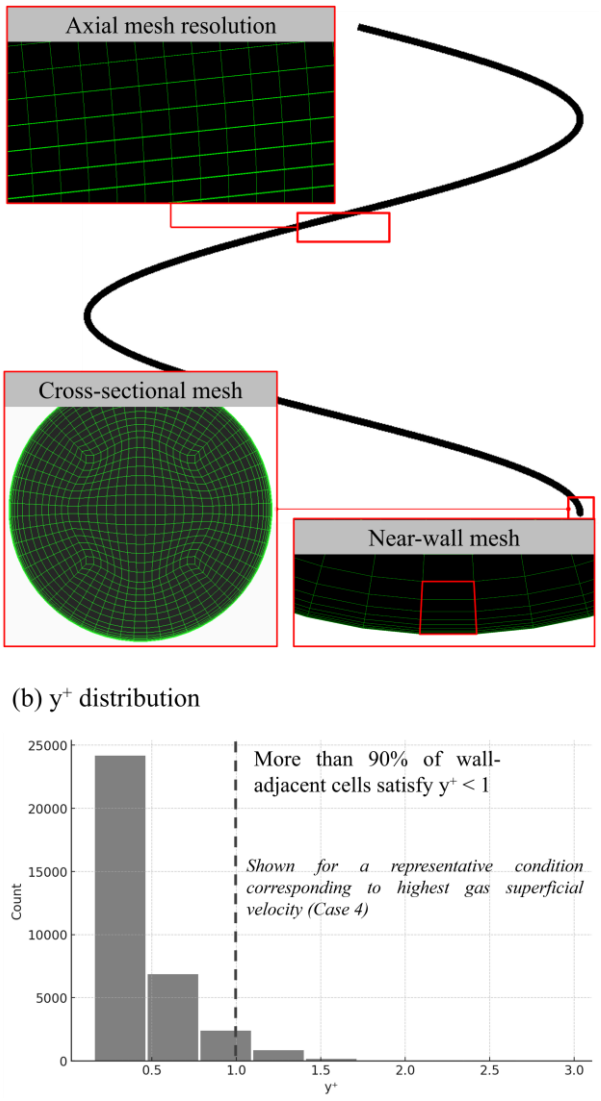

Figure 2. Computational mesh and near-wall resolution.

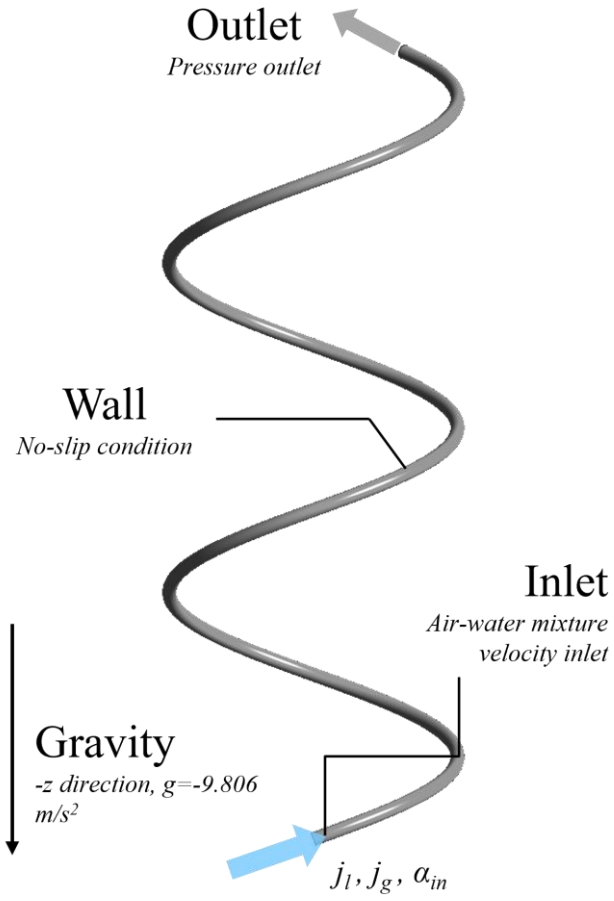

Figure 3. Boundary condition

of wall-adjacent cells), and the sensitivity analysis focused on axial mesh size and timestep, which are known to strongly affect interface resolution and bubble coalescence/breakup behavior in two-phase flows.

First, the sensitivity to axial mesh resolution was examined by varying the axial mesh size while keeping all other numerical and physical conditions identical. Figure 4 presents an example of instantaneous bubble distributions obtained with different axial mesh sizes under the same operating condition, illustrating that coarse axial resolution can alter the representation of bubble deformation, coalescence, and breakup. To quantify this effect, time-averaged void fraction and time-averaged pressure drop were evaluated for each axial mesh configuration, as shown in Figure 5. Both quantities exhibit limited variation for axial mesh sizes finer than 1–2 mm, and the axial mesh size of 1 mm was selected as eswka compromise between numerical accuracy and computational cost, yielding variations within approximately 5.6% for void fraction and 1.48% for pressure drop.

Subsequently, timestep sensitivity was assessed using the selected axial mesh size. Because globally averaged quantities showed only minor differences among the tested time steps, the analysis focused on the axial distribution of time-averaged void fraction, which is more sensitive to transient interface dynamics. Figure 6 compares the time-averaged void fraction profiles along the axial direction for different timestep sizes after the flow reached a statistically stationary state. The results indicate that the void fraction distributions converge as the time step decreases, while the pressure distribution along the coil exhibits negligible differences among the tested cases. Based on these observations, a time step of 0.4ms was adopted for all subsequent simulations, providing sufficient temporal resolution with acceptable computational cost.

3. Result and Discussion

Figure 7 compares the time histories of cross-sectionally averaged void fraction obtained from the experiment and CFD. The comparison was performed over the same 2 s interval for each case, and the time-averaged void fraction α_{avg} is indicated in each panel. The purpose of this comparison is not to assess point-by-point phase agreement in time, but to evaluate whether CFD reproduces the unsteady two-phase flow behavior,

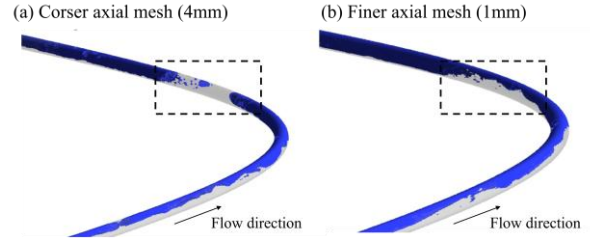

Figure 4. Representative instantaneous bubble distributions for different axial mesh sizes.

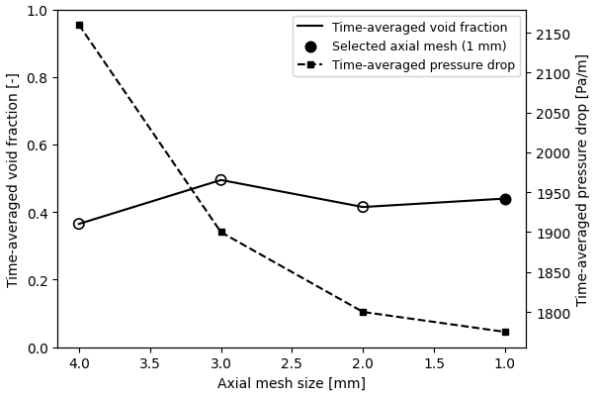

Figure 5. Axial mesh sensitivity analysis for time-averaged void fraction and pressure drop

including the overall waveform pattern and the mean void-fraction level.

As shown in Figure 7, CFD reproduced the unsteady void-fraction fluctuations in all cases. In Case 1, intermittent spike-like signals were observed under a low mean void-fraction condition, and CFD captured a similar intermittent behavior, although the predicted mean void fraction was slightly higher than the experimental value. In Cases 2 and 3, periodic fluctuation patterns were more clearly observed, and CFD generally reproduced the cyclic behavior and the fluctuation range of void fraction. In Case 4, a high void-

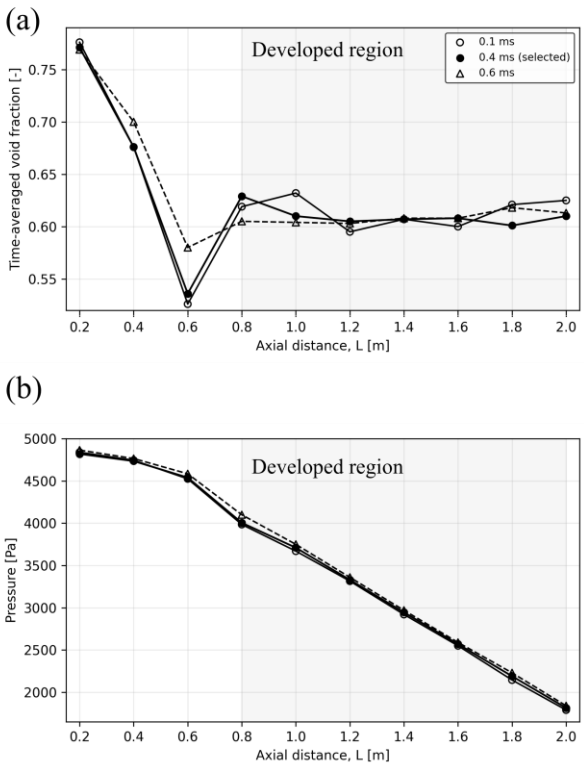

Figure 6. Timestep sensitivity analysis with the selected axial mesh size (1 mm): (a) axial time-averaged void fraction and (b) axial pressure for different timestep sizes.

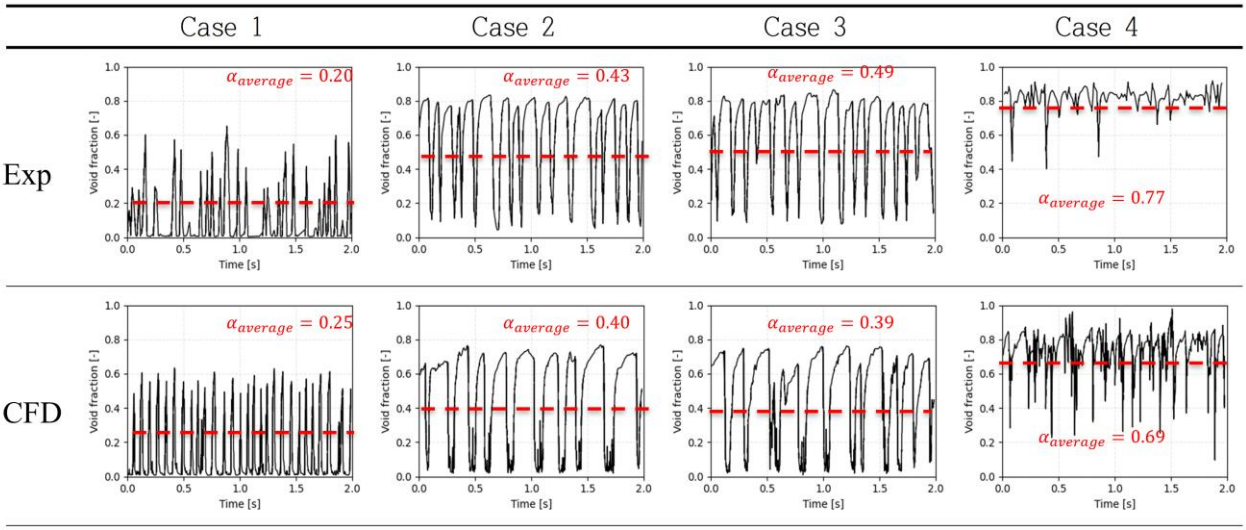

Figure 7. Time histories of cross-sectionally averaged void fraction for the experiment and CFD (Cases 1–4, 2 s interval).

fraction level with superimposed unsteady fluctuations was observed, and CFD showed a similar mean level and fluctuation pattern. Differences are still observed in the detailed waveform features, such as peak sharpness, duration of low-void intervals, and instantaneous fluctuation amplitude. These differences are attributed to the inherently unsteady nature of two-phase flow and the phase-sensitive characteristics of the signals.

To further evaluate the fluctuation behavior, a fast Fourier transform (FFT) was applied to the cross-sectionally averaged void-fraction signal $\alpha(t)$, and the experiment and CFD were compared in the frequency domain (Figure 8). The same 2 s time interval was used for all cases, resulting in a frequency resolution of $\Delta f = 1/T = 0.5$ Hz. For the discrete time series $\alpha_n = \alpha(t_n)(n = 0, \dots, N-1)$, the FFT was computed as

$$X_k = \sum_{n=0}^{N-1} \alpha_n \exp\left(-i\frac{2\pi kn}{N}\right),\ f_k = \frac{k}{N\Delta t} \qquad (6)$$

where $| X_k |$was used as the spectral magnitude of the void-fraction signal. The dominant frequency was defined as the frequency with the maximum spectral magnitude within 1–100 Hz:

$$f_{\text{peak}} = \underset{1 \le f_k \le 100}{\arg\max} | X_k | \qquad (7)$$

Because a single dominant frequency does not fully represent the overall spectral shape, cosine similarity was additionally introduced to quantify the similarity of the full spectrum pattern in the same frequency range (1–100 Hz). Let $\mathbf{x}_{\text{EXP}}$ and $\mathbf{x}_{\text{CFD}}$ denote the spectral magnitude vectors of the experiment and CFD, respectively. The cosine similarity is defined as

$$Cosine\ Similarity = \frac{\mathbf{x}_{\text{EXP}} \cdot \mathbf{x}_{\text{CFD}}}{\| \mathbf{x}_{\text{EXP}} \| \ \| \mathbf{x}_{\text{CFD}} \|} \qquad (8)$$

The FFT results in Figure 8 show that the main spectral peaks are well matched in Cases 2 and 4, indicating good reproduction of the dominant oscillation period by CFD. In Case 1, the overall energy distribution and major peak structure in the low-frequency range are also similar, although the exact peak locations and amplitudes differ because of the intermittent signal characteristics. In Case 3, the dominant frequency showed a relatively large discrepancy, suggesting that the dominant-period metric can be sensitive under this flow condition. However, even in Case 3, the overall spectral distribution from low to intermediate frequencies remained similar between the experiment and CFD. This indicates that CFD reproduced the overall fluctuation signature of the flow, even when the dominant frequency alone did not match closely.

Table 4 summarizes the quantitative comparison metrics from both the time-domain and frequency-domain analyses. The absolute difference in time-averaged void fraction, $| \alpha_{avg,\text{EXP}} - \alpha_{avg,\text{CFD}} |$, was 0.05, 0.03, 0.10, and 0.08 for Cases 1–4, respectively, indicating generally good agreement in the mean void-fraction level. For the dominant frequency comparison,

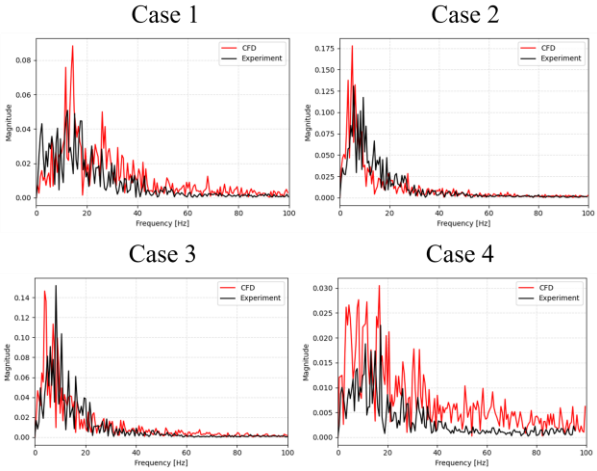

Figure 8. FFT spectra of void-fraction signals for the experiment and CFD (Cases 1–4).

the relative errors in Cases 2 and 4 were 9.37% and 2.97%, respectively, showing good predictive performance for the representative oscillation period. Case 1 also showed a moderate difference (16.53%), whereas Case 3 exhibited a larger error (53.35%). In contrast, the cosine similarity remained within 0.779–0.851 for all cases, with particularly high values for Cases 2 and 4 (0.847 and 0.851, respectively). Even in Case 3, where the dominant frequency error was large, the cosine similarity was 0.779, indicating that the overall spectral pattern was still reasonably reproduced.

Overall, the present CFD results for two-phase flow in the helical coil show good reproducibility in terms of both the time-averaged void fraction (mean metric) and the FFT-based spectral pattern (phenomenon-based metric). However, the large dominant-frequency error in Case 3 also shows that a single peak-based metric is not sufficient to fully evaluate CFD performance for all flow conditions. Therefore, a multi-metric validation framework, combining mean void fraction, dominant frequency, and spectral pattern similarity, is effective for assessing CFD reproducibility of helical-coil two-phase flow. The present results also provide a practical basis for defining the applicable validation range of CFD in design and analysis of helical-coil systems.

Table 4. Quantitative validation metrics for the experiment–CFD comparison

Case num	$f_{peak,Exp}$ [Hz]	$f_{peak,Exp}$ [Hz]	Cosine Similarity	$\Delta\alpha_{avg}$
1	12.40	14.45	0.790	0.05
2	5.55	5.03	0.847	0.03
3	8.36	3.90	0.779	0.10
4	17.20	16.69	0.851	0.08

4. Conclusion

This study performed a quantitative validation of transient CFD predictions for air–water two-phase flow in a helical coil using experimentally obtained void-fraction data over multiple flow regimes. The comparison was conducted using both time-domain and frequency-domain analyses of the cross-sectionally averaged void fraction signal.

The time-history comparison showed that CFD reproduced the unsteady fluctuation behavior and the overall mean void-fraction level in all tested cases. Although differences were observed in detailed waveform features, such as instantaneous peak shape and local fluctuation amplitude, the overall unsteady patterns were generally captured. The absolute difference in time-averaged void fraction between the experiment and CFD remained within a relatively small range across all cases.

To further evaluate the fluctuation characteristics, FFT-based analysis was performed, and both the dominant frequency and spectral-pattern similarity were examined. The dominant frequency was well predicted in some cases, while a relatively large discrepancy was observed in one case. However, the cosine similarity of the spectra remained reasonably high for all cases, indicating that CFD reproduced the overall fluctuation signature even when the dominant frequency did not match closely.

These results show that validation based only on a single metric is not sufficient for helical-coil two-phase flow. A multi-metric validation approach combining mean void fraction, dominant frequency, and spectral-pattern similarity was found to be effective for assessing CFD reproducibility. The present results provide a practical basis for defining the applicable validation range of CFD for helical-coil two-phase flow analysis.

5. Acknowledgement

This work was supported by the Innovative Small Modular Reactor Development Agency grant funded by the Ministry of Science and ICT(No. RS-2024-00408520).

REFERENCES

[1] Prabhanjan, D. G., Raghavan, G. S. V., and Rennie, T. J., “Comparison of Heat Transfer Rates Between a Straight Tube Heat Exchanger and a Helically Coiled Heat Exchanger,” *International Communications in Heat and Mass Transfer*, Vol. 29, No. 2, 2002, pp. 185–191. doi:10.1016/S0735-1933(02)00309-3.

[2] Flayyih, R. A., Alwan, K. J., and Aljaberi, H. A., “Comparative Heat Transfer Analysis of Helical Coil and Straight Tube Heat Exchangers,” *Case Studies in Thermal Engineering*, Vol. 76, 2025, 107386. doi:10.1016/j.csite.2025.107386

[3] Zhu, Hongye, et al. "Flow regime identification for upward two-phase flow in helically coiled tubes." *Chemical Engineering Journal* 308 (2017): 606-618.

[4] Zhu, Guangyu, et al. "Intermittent gas-liquid two-phase flow in helically coiled tubes." *International Journal of Multiphase Flow* 116 (2019): 113-124.

[5] Breitenmoser, David, et al. "High-resolution high-speed void fraction measurements in helically coiled tubes using X-ray radiography." *Nuclear Engineering and Design* 373 (2021): 110888.